Journal of Zhejiang University-SCIENCE A (Applied Physics & Engineering) 2025 26(4):359-375
www.jzus.zju.edu.cn; www.springer.com/journal/11582
E-mail: jzus_a@zju.edu.cn

Research Article

https://doi.org/10.1631/jzus.A2400068

Impact of disc-cutter partial wear on tunneling parameters and a high-accuracy method for discrimination of partial wear

Xinghai ZHOU[1,2], Yakun ZHANG[1]✉, Guofang GONG[1], Huayong YANG[1]

[1]*State Key Laboratory of Fluid Power & Mechatronic Systems, Zhejiang University, Hangzhou 310058, China*
[2]*Power China Huadong Engineering Co., Ltd., Hangzhou 311122, China*

Abstract: In tunnel construction with tunnel boring machines (TBMs), accurate knowledge of disc-cutter failure states is crucial to ensure efficient operation and prevent delays and cost overruns. This study investigates the influence of disc-cutter partial wear on tunneling parameters and proposes a novel method for discriminating partial-wear ratio based on a stacking ensemble model. The time-domain features of torque and thrust, including the average value and standard deviation, are analyzed through a series of scaled-down experimental tests on partial wear. Torque and thrust values will increase when a disc cutter is trapped and partially worn. The impact of partial-wear ratio on tunneling parameters appears to be more significant than partial-wear depth. A total of 40 features are selected from the time domain, frequency domain, and time-frequency domain to describe the torque and thrust. The relationships between these features and the partial-wear ratio are analyzed using the Pearson coefficient and Copula entropy. The results reveal that, except for the form factor in the time-domain features, the remaining features exhibit certain linear or non-linear correlations with the partial-wear ratio. Lastly, the proposed model successfully achieves the discrimination of the partial-wear ratio and outperforms other commonly used models in terms of overall classification accuracy and differentiation capability in different categories. This research provides effective support for monitoring and health management of disc-cutter failure states.

Key words: Tunnel boring machine (TBM); Disc cutter; Partial wear; Tunneling parameters; Multi-domain features; Ensemble learning

1 Introduction

Disc cutters are critical components of tunnel boring machines (TBMs) and play a vital role in the success of tunneling operations (Farrokh and Rostami, 2008; Bilgin and Algan, 2012). Despite being designed for harsh and unpredictable underground conditions (Zhang and Xiao, 2018a), disc cutters often experience high failure rates due to the high stresses and abrasion they encounter during operation (Acaroglu et al., 2008; Zhang and Xiao, 2018b; Yu et al., 2020). If a failed disc cutter is not replaced in time, it can lead to the failure of adjacent disc cutters and even damage to the cutterhead. Because of these high failure rates and the severe consequences, it is crucial to gather information about the health status of cutters and replace the damaged ones in a timely manner (Yu et al., 2021). However, the current maintenance strategy for disc cutters still relies on periodic manual inspection (Hassanpour et al., 2014). This method requires shutting down the TBM and sending maintenance personnel into the TBM cutterhead. This not only poses significant safety risks, reduces TBM utilization, and increases construction costs (Wang et al., 2019), but it is also highly inefficient. Regular maintenance often results in either insufficient or excessive replacement of disc cutters. Statistics reveal that cutter consumption accounts for one-third of the total cost of tunnel construction, and the time spent on cutter inspection and replacement amounts to approximately one-third of the total project time (Li et al., 2018; Lan et al., 2019). To address this problem, the development of disc-cutter failure detection and early warning technology has received significant research attention.

✉ Yakun ZHANG, ykzhang@zju.edu.cn
Xinghai ZHOU, https://orcid.org/0000-0002-3148-607X
Yakun ZHANG, https://orcid.org/0000-0002-1667-8700

Received Feb. 1, 2024; Revision accepted May 21, 2024; Crosschecked Mar. 13, 2025

The state-of-the-art disc-cutter fault-detection methods can be broadly classified into two categories: sensor-based real-time monitoring and data-driven prediction. The harsh operating conditions and limited installation space pose significant challenges to the development and application of sensor-based technologies. Additionally, the high cost of sensors and difficulties in signal transmission make it challenging to implement these technologies in actual construction sites, limiting their usage only in laboratory environments (Liu et al., 2017). Data-driven approaches, on the other hand, aim to predict disc-cutter status via the excavation data (Li and Su, 2010; Yang and Qiu, 2016; Amoun et al., 2017). For instance, Hassanpour (2018) developed a relationship between cutter life and two main rock parameters including average mineral hardness and intact rock uniaxial compressive strength (UCS), and presented an empirical model for predicting average cutter life using the measured parameters of UCS and the Vickers hardness number of rock. Karami et al. (2021) estimated the cumulative volumetric mass loss of disc cutters based on the compressive strength index and rock-quality designation, and provided a chart to determine the wear on the disc cutters. These data-driven models, which are built by means of statistical analysis of large datasets, indicate that excavation parameters contain valuable information regarding the interaction mechanisms between worn disc cutters and rocks, enabling effective wear prediction. However, these studies primarily focus on normal wear, and there is a serious lack of research on abnormal damage, which is quite common in practice.

Unlike the gradual material removal observed in normal wear (Lin et al., 2020; Pan et al., 2020), abnormal damage occurs in various forms, such as partial wear, fracture, and edge curling (Zhang et al., 2017; Ren et al., 2018). Partial wear is the most common type of abnormal damage (Huang, 2021). Taking the tunneling project of Gaoligong Mountain in China as an example, partially worn cutters accounted for 58.3% of the total number of abnormally damaged cutters and 18.2% of the total worn cutters (Zhang, 2021), as illustrated in Fig. 1. Fig. 2 depicts the partial-wear state of the cutterhead from a decommissioned TBM. The consequences of such damage are significantly more severe compared to normal wear (Su et al., 2020). During the partial-wear process, the cutter ring is quickly and partially worn due to cutter-bearing failure or foreign objects obstructing rotation around the cutter shaft, resulting in only a portion of the cutter contacting with the rock (Ko and Lee, 2020). The transition from a rolling to a sliding motion between the cutter ring and the rock surface intensifies the wear at the contact point, accelerating the wear rate of adjacent disc cutters and leading to premature failure (Sun et al., 2023). If partially worn cutters are not replaced promptly, it can eventually jeopardize the entire cutterhead and drive system. This poses significant safety risks and can result in substantial economic loss.

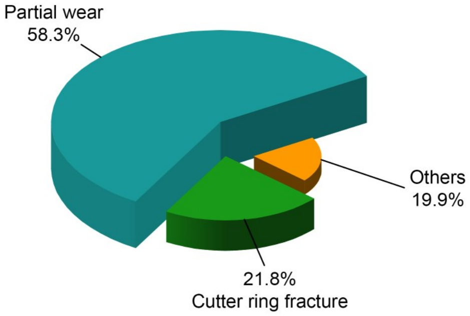

Fig. 1 Proportion of partially worn cutters out of total abnormally damaged cutters

Fig. 2 Partially worn cutters in cutterhead

To assess the impact of partial wear, Sun et al. (2022, 2023) conducted rock-cutting experiments and analyzed the changes in cutting force, rock fragmentation, and energy consumption. However, this research focused only on individual disc cutters, neglecting the influence of the quantity and extent of partial wear on the overall loading of the TBM. There is a notable deficiency in systematic research on partial wear. Knowledge gaps persist regarding the alterations in tunneling parameters following partial wear, real-time and efficient detection of partial-wear occurrence, and evaluation of the degree of partial wear.

In order to fill these gaps, we investigated the differences in tunneling parameters between partially worn and normal disc cutters and developed models to evaluate partial-wear ratio, which will aid in construction operations and maintenance.

The remainder of this paper is organized as follows: We carry out a series of experiments on both normal and partially worn cutters, based on a reduced-scale shield-test rig. Next, the acquisition and analysis of tunneling parameters, specifically torque and thrust, under different failure modes are covered. Finally, a high-performance discrimination method of partial-wear ratio (based on ensemble learning) is proposed and our efforts to verify it are outlined, leading to some conclusions.

2 Experiment and analysis

The experimental setup and procedure for investigating the partial wear of disc cutters are described in this section. Accurate and reliable excavation parameters were obtained through a meticulously designed experimental setup that was capable of reproducing the excavation process. The procedure was a systematic approach to conducting the experiments and capturing the wear patterns observed in the disc cutters. Additionally, we performed a comprehensive analysis to further interpret the experimental results.

2.1 Experimental setup

The tunneling process of a TBM involves numerous operational parameters that are challenging to scale down entirely. This study focused on experiments related to partial wear, with a reduced-scale shield-test rig. Key parameters under investigation included cutterhead and disc-cutter size and material, thrust force, advance speed, cutterhead rotation speed, and cutterhead torque. The technical specifications of the test rig and the TBM used at the Zhengzhou Metro construction site adhered to the following scaling criteria: (1) The materials of the cutterhead and disc cutters on the test rig matched with those of the actual TBM. The actual TBM had a diameter of 6000 mm, while the measured diameter of the test rig was 350 mm, resulting in a geometric scale ratio of 17:1. Additionally, the actual disc cutter had a diameter of 483 mm, whereas the measured diameter of the test disc cutter is 48.3 mm, resulting in a geometric scale ratio of 10:1. (2) Test-rig thrust force was proportional to the TBM's actual thrust force. (3) The advance speed of test-rig aligned with that of actual TBM. (4) Cutterhead torque in the test rig was proportional to the TBM's actual cutterhead torque. (5) Cutterhead rotation speed in the test rig matched with the actual rotation speed of the TBM.

Fig. 3 illustrates the test rig, consisting of a hydraulic system, shield, and rock-soil container. Table 1 details the main technical specifications of the test rig. The horizontal movement of the shield was controlled by the hydraulic system, while the rotation was driven by a servo motor. The cutterhead was installed at the front of the shield machine, and the normal and partially worn disc cutters were arranged on it using bolts.

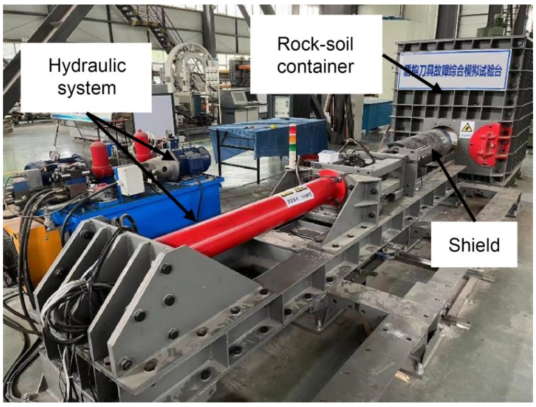

Fig. 3 Reduced-scale shield-test rig for experiments on partial wear

Table 1 Main technical specifications of the test rig

Technical parameter	Design value
Overall dimensions (mm)	4300×866×1300
Cutterhead diameter (mm)	350
Disc-cutter diameter (mm)	48.3
Maximum stroke (mm)	1300
Cutterhead rotation speed (r/min)	0–10
Maximum allowable torque (N·m)	1000
Advance speed (mm/min)	0–50
Dimensions of rock-soil container (mm)	1200×1500×1500

The compound cutterhead was specifically designed to primarily drive the rotation of the disc cutters for rock-breaking, as depicted in Fig. 4a. It can be seen that there are 15 cutter seats distributed on the cutterhead, of which 12 are equipped with 12 face disc cutters, evenly distributed at an angle of 60°; the outer circle has three seats equipped with three edge disc cutters, distributed at an angle of 120° and tilted at an angle of 10°. For convenience of description, the 15 disc cutters are numbered and their installation radii are shown in Fig. 4a and Table 2. Numbers 1 to 12 are face disc cutters, and numbers 13 to 15 are edge disc cutters. The scrapers are also divided into three groups at an angle of 120°, with eight in each group, and installed on the opening edge of the cutterhead. The dimensions of the scrapers were scaled down to a ratio of 1:10, following the general practice in engineering.

In engineering applications, partial wear of disc cutters is typically caused by bearing failure or obstructions preventing rotation around the cutter shaft, causing a relative motion transition from rolling to pure sliding between the cutter and the rock (Zhang, 2011). To faithfully recreate the substantial disparities between normal and partially worn cutters, we used effective structural designs for the experimental cutter seat and disc cutter. Fig. 5 illustrates that the cylindrical ends of the normal cutter were replaced with a square structure and the cutter seat was modified as well, which enabled the cutter to be jammed during the shield tunneling process, resulting in a "trapped cutter". In this case, the cutter ring did not undergo any wear. When the outer contour of the cutter no longer exhibits a complete circular shape, it is referred to as a partially worn cutter (as shown in Fig. 6). The geometric profile of the contact area can be divided into two regions: the arc surface and the plane. The depth of partial wear is defined as the difference between the radius and the perpendicular distance from the disc cutter's center

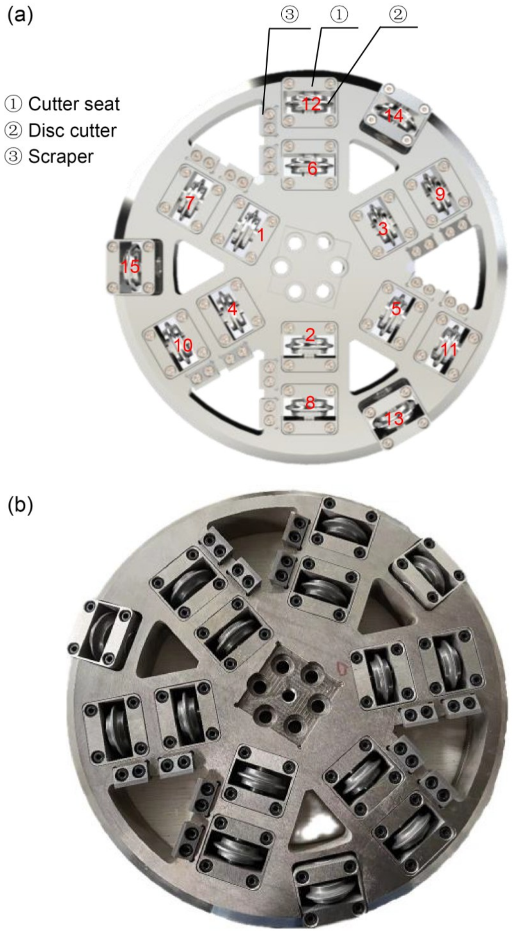

Fig. 4 (a) Schematic structure and disc-cutter numbering diagram; (b) assembly of the cutterhead

Table 2 Installation radius of 15 disc cutters

Number	Installation radius (mm)	Number	Installation radius (mm)
1	65	9	130
2	70	10	135
3	75	11	140
4	80	12	145
5	85	13	147
6	90	14	149
7	120	15	151
8	125		

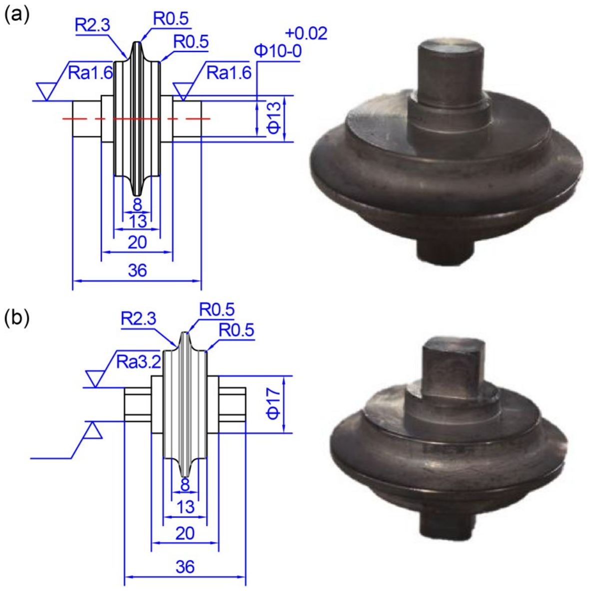

Fig. 5 Structural design of disc cutters (unit: mm): (a) normal cutter; (b) trapped cutter

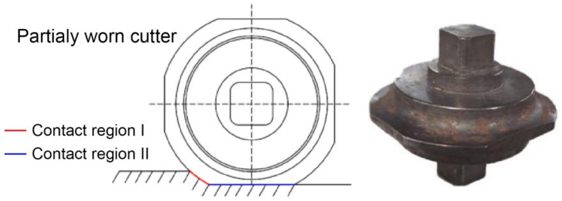

Fig. 6 Partially worn cutter. References to color refer to the online version of this figure

to the contact plane. To simulate this scenario accurately, the designed cutters were subjected to linear cuts, creating a flat surface on one side, mimicking the effect of partial wear. Various depths of partial wear were then simulated by successively removing 0.5 mm, 1.0 mm, 1.5 mm, and 2.0 mm from the cutting ring. The corresponding real partial-wear depths are 5 mm, 10 mm, 15 mm, and 20 mm.

A composite strata consisting of soft soil on the top and sandstone on the bottom was selected for shield tunneling and placed in the rock-soil container. All the materials used in the experiments were collected from the same construction site of the Zhengzhou Metro to ensure the consistency of composition and strength. The rock-soil properties are presented in Table 3. The dimensions of the rock-soil container were 1200 mm×1500 mm×1500 mm, significantly larger than the excavation diameter of the shield, thereby eliminating the influence of limited boundaries in the experiments. To enable real-time excavation-data collection, we implemented a comprehensive data-acquisition and monitoring system. This system recorded various parameters, including cutterhead speed, advance speed, and cutterhead torque and thrust, at a sampling frequency of 1 Hz. High-precision torque sensors (0–1000 N·m) and wheel-type pressure sensors (0–80 t) were used to measure the cutterhead torque and thrust, respectively. The cutterhead speed and advance speed were obtained from the signal output ports of a servo motor driver.

Table 3 Properties of the experimental materials

Property	Value	
	Soft soil	Sandstone
Moisture content (%)	9.86	6.60
Porosity	60.4	6.6
Compressibility	0.57	0.64
Internal friction angle (°)	26.0	27.2
Cohesive strength (kPa)	26	28
Shear modulus (kPa)	15	18

2.2 Experimental procedure

The experimental procedure is detailed in Section S1 of the electronic supplementary materials (ESM).

In order to investigate the impact of partial wear on excavation parameters, we established a total of seven test groups, each consisting of varying proportions of failed cutters and different depths of partial wear. The detailed parameters for each test group are provided in Table 4. In practical engineering, it has

Table 4 Disc-cutter parameters of the test groups

Index	Proportion of failed cutters (%)	Number	Type of cutter	Partial-wear depth (mm)
1#	0	1–15	Normal	0.0
2#	25	10–12	Trapped	0.0
3#-1	25	10–12	Partially worn	0.5
3#-2	25	10–12	Partially worn	1.0
3#-3	25	10–12	Partially worn	1.5
3#-4	25	10–12	Partially worn	2.0
4#	50	7–12	Trapped	0.0
5#-1	50	7–12	Partially worn	0.5
5#-2	50	7–12	Partially worn	1.0
5#-3	50	7–12	Partially worn	1.5
5#-4	50	7–12	Partially worn	2.0
6#	75	4–12	Trapped	0.0
7#-1	75	4–12	Partially worn	0.5
7#-2	75	4–12	Partially worn	1.0
7#-3	75	4–12	Partially worn	1.5
7#-4	75	4–12	Partially worn	2.0

been observed that disc cutters installed farther away from the center of the cutterhead experience a higher probability of failure (Li, 2021). Thus, the arrangement of failed cutters was from the outer periphery to the inner ring of the cutterhead, with an increasing proportion of failures. Each test group was repeated three times, with an excavation distance of 10 mm per repetition. The average values were calculated and reported as the final results of this paper.

2.3 Experimental results and analysis

Excavation parameters have been widely adopted in various models to investigate the interaction mechanisms between disc cutters and rock (Yang et al., 2021). Among them, the thrust along the tunnel axis and the cutterhead torque around it are considered to represent the excavation load of a cutter group and are regarded as the key indicators for measuring the tunneling efficiency of a shield. The former represents the cumulative sum of the normal forces applied to all disc cutters, while the latter corresponds to the cumulative sum of the product of the rolling forces acting on the disc cutters and their respective installation radii. Consequently, the variations in these two parameters reflect the changes in the cutting forces of the disc cutters, serving as indicators of disc-cutter health status.

Fig. 7 illustrates the torque and thrust curves for different types of disc cutters. It can be seen that during the initial stage of shield tunneling, these two parameters rapidly increased and tended to stabilize, while exhibiting periodic fluctuations. This phenomenon is consistent with the experimental observations of disc-cutter pressure distribution conducted by Rostami (2013) and the simulation results based on the discrete/finite-element models by Labra et al. (2017). Additionally, She et al. (2022) confirmed the contribution of dense core to the variations in cutting forces during rock-cutting processes. These findings indicate that

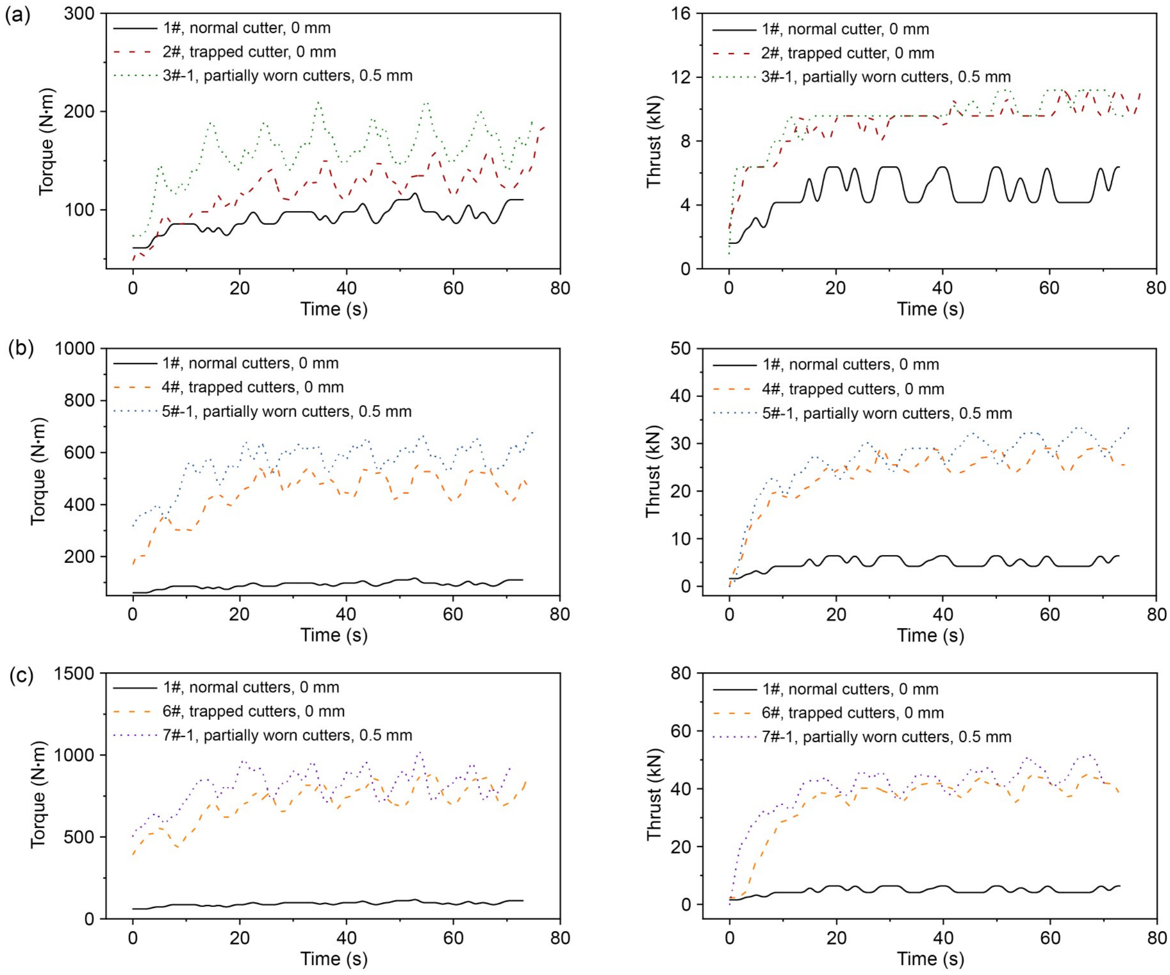

Fig. 7 Variation of torque and thrust of different proportions of failed cutters: (a) 25%; (b) 50%; (c) 75%

the rapid increase in cutting forces is primarily due to the elastic-plastic deformation experienced by the disc cutter upon initial contact with the rock. As the rock approaches its strength limit, it begins to fracture, resulting in a sharp decrease in cutting forces. Consequently, the rock-breaking load exhibits a periodic fluctuation pattern during excavation. When normal cutters become trapped and unable to rotate, the torque and thrust experience a significant increase (1#, 2#, 4#, and 6#), leading to a substantial decrease in the rock-breaking efficiency of the cutters. With regard to the cutter's rock-breaking mechanism, the change in motion pattern increases the sliding friction force, which is much greater than the rolling friction force, thereby significantly increasing the rolling forces exerted by the cutters and resulting in increased torque. The alteration in the geometric shape of the cutter's contact area influences the rock-fragmentation mode, causing the accumulation of rock powder in the plane (contact region II in Fig. 6) and consequently increasing the normal force, which leads to an increase in thrust. When the contact areas on the trapped cutters begin to develop wear, the length of the plane increases with the depth of partial wear, further enlarging the sliding friction between the cutters and the rock and resulting in slight increases in thrust and torque (2# and 3#-1, 4# and 5#-1, and 6# and 7#-1). However, compared to the failure of normal cutters, these changes are relatively minor.

Fig. 8 presents the average values and standard deviations of torque and thrust obtained for each test group (as shown in Fig. 7), which are statistical features of the data signals in the time domain. The torque and thrust were the smallest in all cases where the cutters were in normal condition. The standard deviations were also the smallest for normal cutters, indicating relatively low fluctuation, with a small difference between the maximum and minimum cutting forces (1#). This could be attributed to the intact circular contact area, which maintained relatively stable contact with the rock. As the number of partially worn cutters increased, indicating a higher failure ratio (25%, 50%, and 75%), noticeable increases in torque and thrust, along with larger standard deviations, were observed (1#, 2#, 4#, and 6#). However, the impact of partial wear (with the same partial-wear ratio) on the standard deviation was found to be insignificant, and in some cases, it even led to a reduction in the standard deviation (4# and 5#-1, 6 and 7#-1). This suggests that enlarging the plane area does not significantly affect contact stability between the cutters and the rock, and has only a minor influence on the extent of load fluctuation.

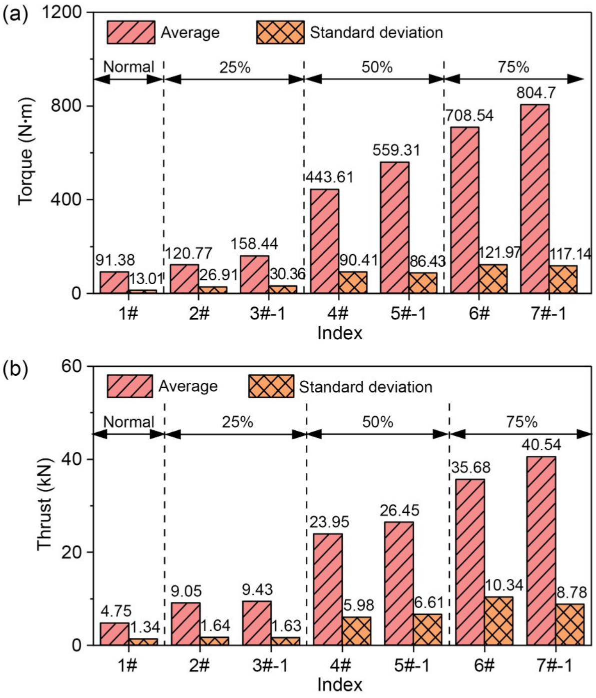

Fig. 8 Average values and standard deviations of torque and thrust for each test group: (a) torque; (b) thrust

The torque and thrust at different partial-wear depths are compared in Fig. 9, providing a more intuitive demonstration of the significant impact of the partial-wear ratio on shield-tunneling parameters. When the ratio was 25% (2#, 3#-1, 3#-2, 3#-3, and 3#-4), both the mean and standard deviation of torque and thrust showed an increasing trend. This is most likely due to the enlarged partial-wear contact area resulting in an increase in the normal forces and sliding friction forces on the cutters. When the partial-wear ratio reached 50% (4#, 5#-1, 5#-2, 5#-3, and 5#-4), the rate of increase in the mean values became slower, and the standard deviation tended to stabilize. Finally, when the partial-wear ratio reached 75% (6#, 7#-1, 7#-2, 7#-3, and 7#-4), fluctuations in torque and thrust were observed at a partial-wear depth of 1 mm. This is probably due to the extreme level of cutter failure, in which the rock-breaking capacity of the shield had reached its limit. At this stage, the front face of the cutterhead was covered by soil and rock, and the advancement of excavation heavily depended on the scrapers and edge cutters positioned along the outer edge of the cutterhead.

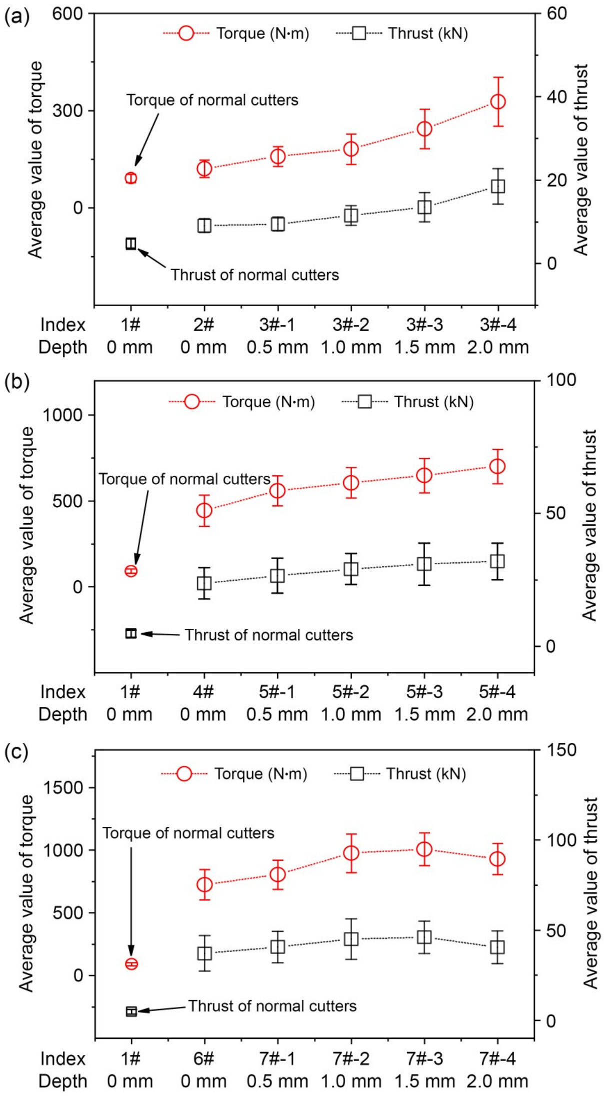

Fig. 9 Average torque and thrust with different partial-wear depths at different proportions of failed cutters: (a) 25%; (b) 50%; (c) 75%

3 Partial-wear-ratio discrimination method and validation

Based on the experimental results analyzed in Section 2.3, we concluded that the partial-wear ratio of disc cutters (i.e., the number of partially worn cutters) has a much greater impact than the degree of wear on tunneling parameters and rock-breaking performance in shield tunneling. The analysis in this section not only focuses on the mean and standard deviation but also extracts additional features from the time domain, frequency domain, and time-frequency domain to reveal their correlations with the partial-wear ratio. Furthermore, we propose and validate an ensemble-learning-based model for partial-wear-ratio discrimination.

3.1 Multi-domain feature extraction

Feature extraction is the process of reducing the dimensionality of raw signal data collected by sensors while preserving the essential information embedded within the data (Huang et al., 2022). Time-domain features, such as average value and standard deviation, are used to gain valuable perspectives into temporal characteristics. By transforming the signals from the time domain to the frequency domain using techniques such as Fourier transform, frequency-domain analysis reveals the underlying frequency content and periodic patterns within the data. Furthermore, integration of time and frequency domains in time-frequency-domain analysis provides understanding of the temporal and spectral characteristics of the torque and thrust signals.

3.1.1 Time domain

The specific features of the time domain include mean, standard deviation, root mean square (RMS), square root amplitude, peak-to-peak, skewness, kurtosis, form factor, crest factor, impulse factor, clearance factor, and energy. These features are calculated using their respective formulas (Liu et al., 2021; Qin et al., 2023), which are detailed in Table S1 of the ESM.

3.1.2 Frequency domain

The objective of frequency-domain analysis is to identify the patterns in the centroid frequency (CF) and root mean square frequency changes of the spectrum as the cutter failure rate varies (Yang et al., 2023). The calculation formulas for frequency-domain features are detailed in Table S2 of the ESM.

3.1.3 Time-frequency domain

Time-frequency-domain analysis utilizes wavelet packet decomposition to decompose the raw signal data into multiple sub-bands. The average energy of each sub-band is then extracted as a feature value. This analysis technique addresses the limitations of the fixed window of Fourier transform in frequency-domain analysis, and enables direct reflection of non-stationary and short-term features. In this study, we employed the ‘db4’ wavelet basis function to perform two-level wavelet packet decomposition on the thrust and torque signal data collected during the tunneling process. This decomposition yielded four sub-band signals. The average energy of the wavelet packet coefficients within each sub-band was computed as the feature parameters. This yielded 4 time-frequency-domain features.

In Fig. 10, time-domain waveforms, spectra, and sub-band energies with different partial-wear ratios are presented, using thrust data as an example. The maximum magnitudes of each time-domain waveform were 9.57, 11.17, 30.63, and 45.30. Like the mean and standard deviation discussed in Section 2.3, these magnitudes increased with the rise in partial-wear ratio. As indicated by the calculation formula of time-domain features, the other nine (e.g., RMS, square root amplitude) were correlated with the mean, standard deviation, and maximum values, thus exhibiting certain relationships with the partial-wear ratio. In the frequency domain, there was a gradual decrease in the magnitudes of frequencies with increasing partial-wear ratio, with minimum values of −46.74, −53.56, −58.32, and −62.99. This observation reveals a negative correlation between the minimum frequency magnitudes and the partial-wear ratio. Furthermore, based on the calculation formula of frequency-domain features, the four features related to magnitudes, namely the CF, average frequency, standard deviation of frequency, and root mean square frequency, also convey information about the changes in partial-wear ratio. Wavelet packet decomposition revealed the energy values of the four sub-bands. Over 99% of the energy was concentrated in the first sub-band. In addition, the energy of the first and second sub-bands increased with increasing partial-wear ratio, while the relationship between the energy of the third and fourth sub-bands and the partial-wear ratio was less apparent. Therefore, these four sub-band energy values can serve as preliminary features but will require further investigation into their specific relationships with partial-wear ratio. To summarize, we focused on the torque and thrust signals during excavation. For each type of data, a total of 12 time-domain features, 4 frequency-domain features, and 4 frequency-domain feature selections were extracted, resulting in a total of 40 features. All the features are shown in Table S3 of the ESM.

3.2 Feature-correlation analysis

In order to investigate the relationship between the features from different domains and partial-wear ratio more comprehensively, we used two correlation analysis methods.

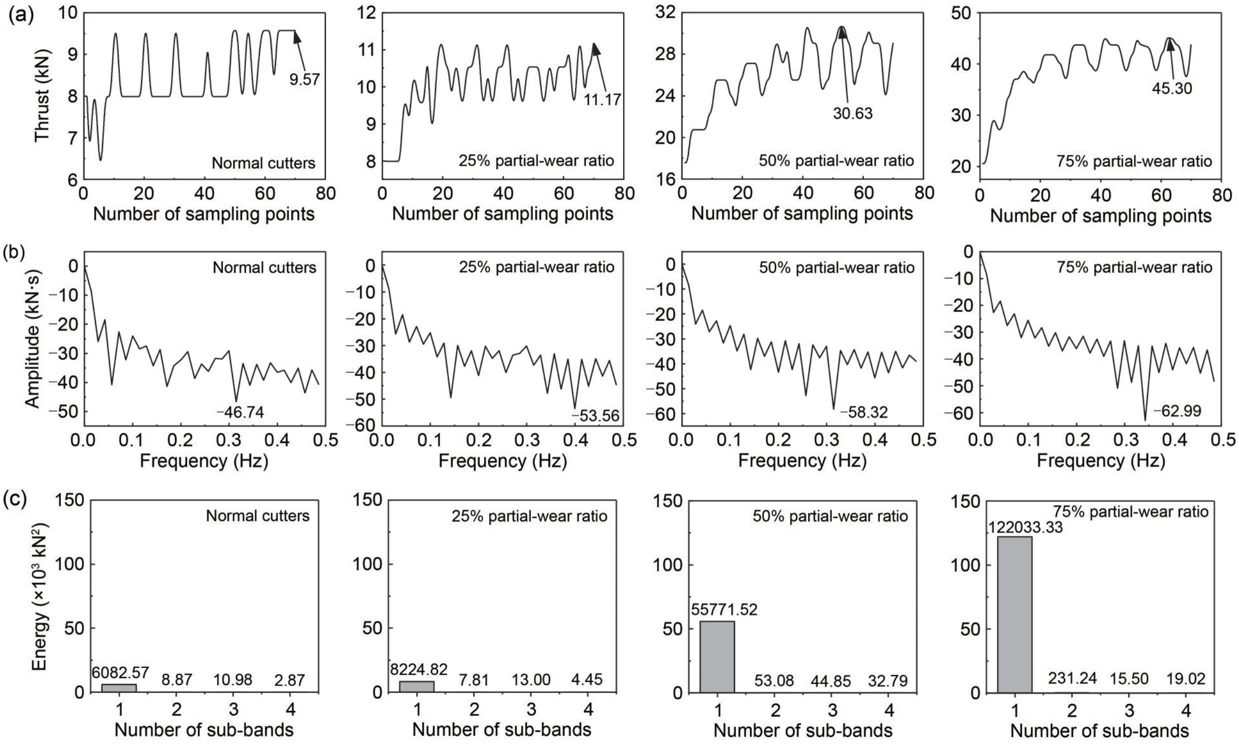

Fig. 10 Multi-domain feature spectrum: (a) time-domain waveforms; (b) spectrograms; (c) sub-band energy diagrams

3.2.1 Pearson correlation coefficient

In statistics, the Pearson correlation coefficient (Jiang et al., 2022; Yu et al., 2023) is a widely used measure to quantify the linear relationship between two variables, typically denoted as *X* and *Y*. It provides a value between 1 and −1, with a value closer to 1 indicating a stronger positive correlation, a value closer to −1 indicating a stronger negative correlation, and a value close to 0 suggesting a weak (or no linear) correlation. The Pearson correlation coefficient is calculated using the following formula:

$$\rho(X,\ Y)=\frac{\operatorname{cov}(X,\ Y)}{\sqrt{\operatorname{var}(X)\cdot\operatorname{var}(Y)}},\tag{1}$$

where $\rho(X,\ Y)$ represents the Pearson correlation coefficient between *X* and *Y*; $\operatorname{cov}(X,\ Y)$ denotes the covariance between *X* and *Y*, which measures the joint variability of the two variables; $\operatorname{var}(X)$ and $\operatorname{var}(Y)$ represent the standard deviations of *X* and *Y*, respectively, which quantify the individual variability of each variable.

In Fig. 11, the Pearson correlation coefficients between the 40 extracted features and the partial-wear ratio are presented. The absolute values of these coefficients indicate the strength of the linear relationship. The results demonstrate a strong positive correlation (approximately >0.5) between the frequency-domain and time-frequency-domain features and the partial-wear ratio. However, the time-domain features related to thrust and torque, such as skewness, kurtosis, form factor, crest factor, impulse factor, and clearance factor (12 features in total), exhibit no or very weak linear correlation. This implies that these features have limited predictive ability for partial-wear ratio, as their absolute correlation coefficients are less than 0.2 (T_{Skewness}, T_{Kurtosis}, $T_{\text{FormFactor}}$, $T_{\text{CrestFactor}}$, $T_{\text{ImpulseFactor}}$, $T_{\text{ClearanceFactor}}$, and F_{Kurtosis}) or close to 0.2 (F_{Skewness}, $F_{\text{FormFactor}}$, $F_{\text{CrestFactor}}$, $F_{\text{ImpulseFactor}}$, and $F_{\text{ClearanceFactor}}$). However, considering that these features are commonly used to describe the skewness, sharpness, peak characteristics, and impulse characteristics of data, their weak linear correlation with partial-wear ratio should be interpreted in the context of their primary use for assessing non-linear signal characteristics. Consequently, further exploration of the non-linear relationships between these features and the partial-wear ratio can be pursued using alternative analysis methods.

3.2.2 Copula entropy

Copula entropy (CE) can also be utilized as a measure of association between multiple variables (Cui and Sun, 2022). CE quantifies the information content in the relationship and is ideal for assessing statistical independence. Unlike traditional measures such as the Pearson correlation, CE does not rely on model assumptions or complexity, and offers significant advantages in terms of universality. Moreover, entropy is a well-defined concept with clear physical interpretation. CE represents the information content in the functional relationship between the independent variables and the target variable, making it easily comprehensible and interpretable from a physical perspective. Its estimation is based on ordinal statistics, which involves no

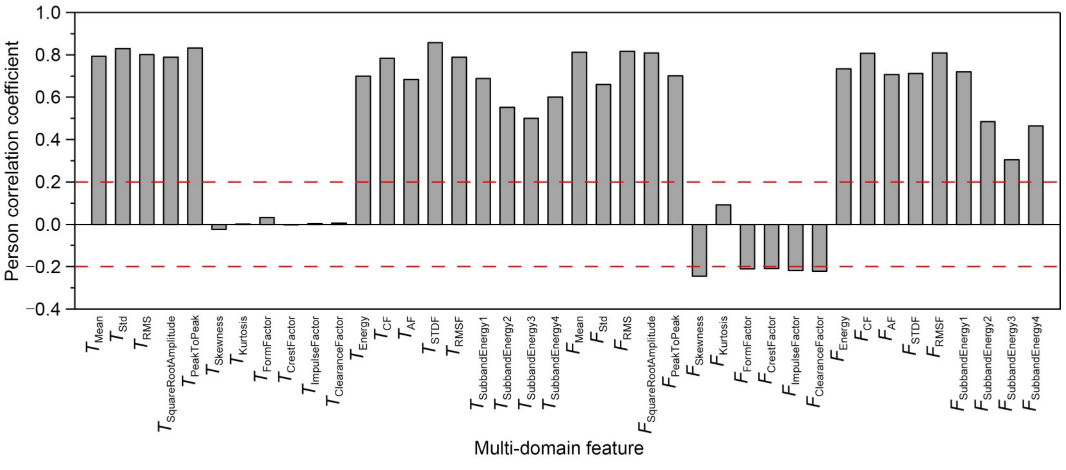

Fig. 11 Pearson correlation coefficients between multi-domain features and partial-wear ratio. The variables are described in Tables S2 and S3 of the ESM

theoretical assumptions and results in good asymptotic stability and minimal parameter tuning.

Fig. 12 showcases the results of calculating CE between the 40 features and the partial-wear ratio. There is a wealth of information regarding the relationship between the partial-wear ratio and the various features in the frequency domain, time-frequency domain, and time domain. The CE values of the 12 features with extremely weak linear correlation, shown in Fig. 12, exhibit noticeable variations. Only the form factor continues to display a remarkably low level of non-linear correlation, while the remaining features demonstrate certain non-linear relationships with the partial-wear ratio. The form factor, which measures the peak characteristics of the signal waveform by comparing the peak value to the effective value, remains unrelated to the partial-wear ratio due to the relatively smooth waveforms and smaller peaks of thrust and torque in this study. Surprisingly, the peak-to-peak value of thrust force (CE: 0.18) shows a lower non-linear correlation compared to its linear correlation (Pearson coefficient: 0.70) with the partial-wear ratio. This unexpected finding may be attributable to the less pronounced periodic fluctuations in thrust. After conducting an analysis of both linear and non-linear correlations, we selected a total of 38 features (excluding the form factor) as effective features for discriminating partial-wear ratio.

3.3 Model for partial-wear-ratio discrimination

3.3.1 Ensemble learning

Ensemble learning is a powerful machine-learning technique that aims to enhance the predictive accuracy and generalization capability of models by combining multiple weaker base models (Shi et al., 2023; Zhang et al., 2023). It has gained considerable popularity in the field of machine learning due to its ability to improve model performance. There are three common types of ensemble learning models: bagging, boosting, and stacking.

Bagging, short for bootstrap aggregating, involves training multiple base models independently in parallel and then aggregating their predictions using a specific strategy. In classification models, the aggregation can be done through voting, while in regression models, averaging is commonly used. The main idea behind bagging is to reduce variance and increase stability by combining the predictions of diverse base models.

Boosting, on the other hand, is a sequential ensemble learning method in which multiple base models of the same type are trained in sequence (Wang et al., 2022). Each subsequent model is trained to correct the prediction mistakes made by previous models. By focusing on the instances that were incorrectly predicted, boosting aims to improve the overall performance of the ensemble model.

Stacking is a more complex ensemble learning technique that involves training multiple base models independently in parallel and then training a meta-model to combine their outputs (Hou et al., 2022). Unlike bagging and boosting, stacking allows for the use of different algorithms to train the base models. The training process of a stacking model typically involves splitting the training dataset into K folds, training different base models K times, and averaging their training results. The outputs of these base models are then

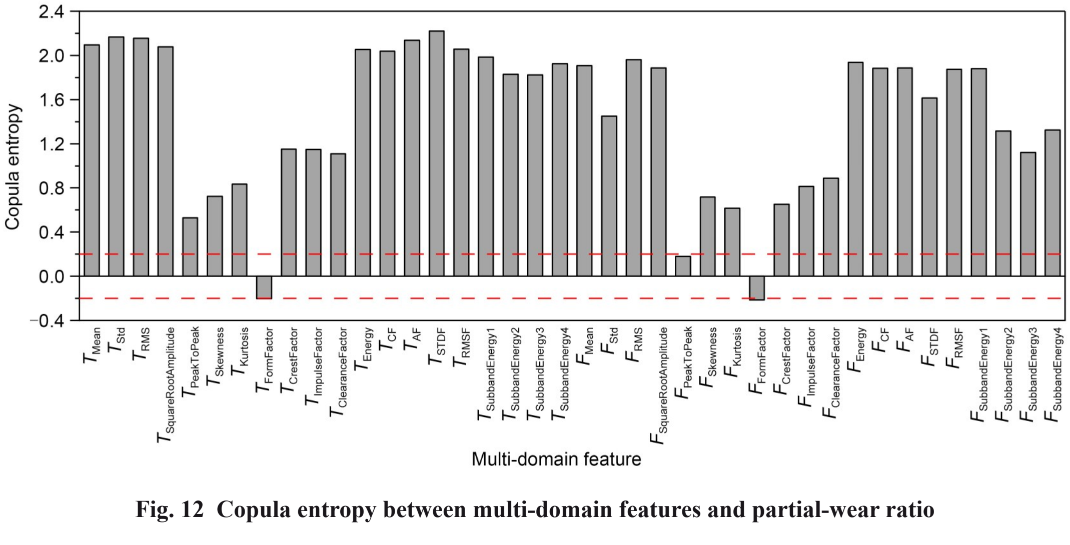

Fig. 12 Copula entropy between multi-domain features and partial-wear ratio

used as input features for the meta-model, which is trained to produce the final prediction.

To prevent overfitting, a simple model such as elastic net regression or logistic regression is often used as the meta-model in ensemble learning. The simplicity of the meta-model helps to generalize the combined predictions of the base models and avoid overfitting the training data. The structure of stacking ensemble learning is shown in Fig. 13. Overall, ensemble learning leverages the strengths of multiple models and mitigates the weaknesses of each individual model, resulting in improved prediction accuracy and generalization.

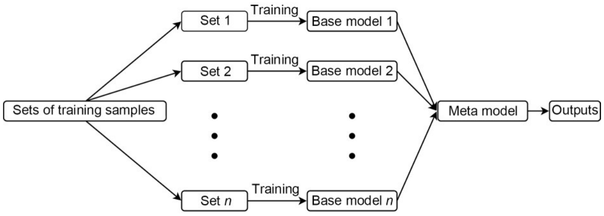

Fig. 13 Structure of stacking ensemble learning

3.3.2 Partial-wear-ratio discrimination model (PRDM)

In this paper, we propose a novel model for predicting the partial-wear ratio of disc cutters, which combines the predictions of multiple base models using stacking ensemble learning. The base models employed in the stacking model include *k*-nearest neighbor (KNN), random forest (RF), support vector classification (SVC), and multilayer perceptron (MLP). These models are trained independently and their outputs are used as input features for the meta-model, which is a logistic regression (LR) model. The specific structure of the model is illustrated in Fig. 14.

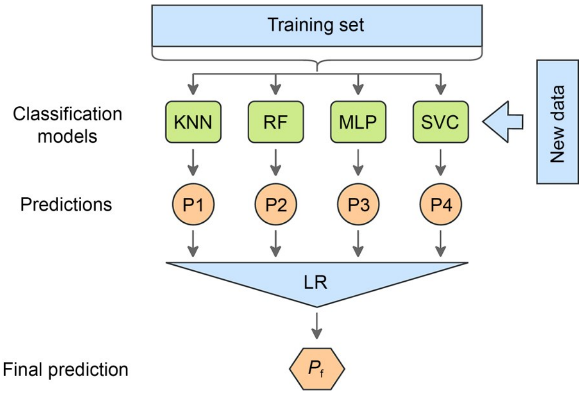

Fig. 14 Specific structure of the PRDM

The ensemble learning model utilizes a feature space consisting of the 38 features discussed in Section 3.2, which serve as input features for the model's dataset. The model's output comprises various partial-wear ratios, including the normal state (1#) as well as ratios of 25% (2#), 50% (4#), and 75% (6#). These states are encoded as 0, 1, 2, and 3, respectively, representing the output categories of the model. To ensure optimal model performance and mitigate issues such as overfitting or underfitting, appropriate hyperparameters must be carefully selected. However, manual hyperparameter selection can be time-consuming and prone to error. To address this, we employed the grid search method, systematically exploring different combinations of hyperparameters and evaluating each combination through cross-validation. In addition, we selected commonly used accuracy evaluation metrics (A) for the models, which represent the ratio of number of correctly categorized samples (N_{CC}) to the total number of samples (N_{T}), as shown in Eq. (2).

$$A=\frac{N_{\mathrm{CC}}}{N_{\mathrm{T}}}. \tag{2}$$

Fig. 15 illustrates the grid-search results for the three base models: KNN, RF, and SVC. For the KNN model, the highest classification accuracy (76.25%) is achieved when the number of neighbors ($n_{\mathrm{neighbors}}$) is set to 7. In the RF model, optimal performance is obtained by setting the number of decision trees ($n_{\mathrm{estimators}}$) to 40 and the maximum depth of each tree ($d_{\max}$) to 4, resulting in an accuracy of 80.96%. For the SVC model, the best result is obtained by adjusting the penalty parameter (C_{svc}) and the width parameter (γ) of the Gaussian kernel. Specifically, a penalty parameter of 1000 and a width parameter of 0.001 yield the optimal outcome (84.56%).

The grid-search results for the MLP model with single-layer and two-layer hidden configurations are presented in Fig. 16. In the case of a single-layer hidden configuration, an accuracy of 88.16% was achieved when the neuron size was set to (60) and the solver was selected as ADAM. For a two-layer hidden configuration with neuron sizes set to (40, 40) and using the ADAM solver, the accuracy slightly decreased to 88.05%, a bit lower than that of the single-layer hidden configuration.

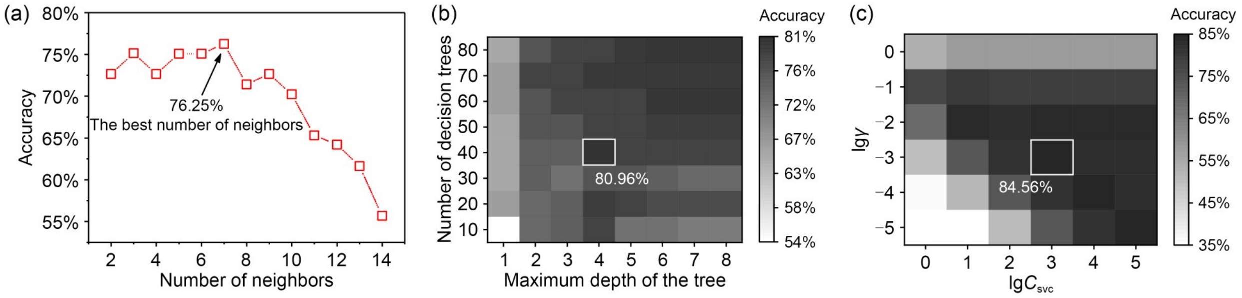

Fig. 15 Grid-search results for the models: (a) KNN; (b) RF; (c) SVC

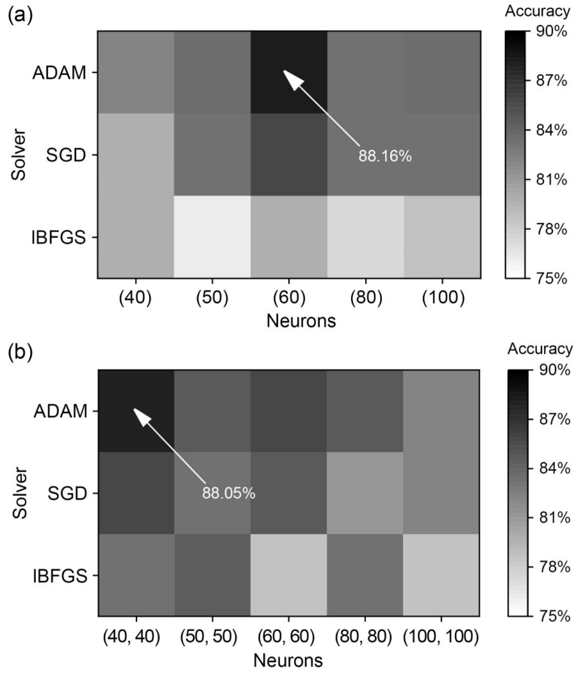

Fig. 16 Grid-search results for the MLP model: (a) single-layer; (b) two-layer. ADAM: adaptive moment estimation; SGD: stochastic gradient descent; IBFGS: limited-memory broyden-fletcher-goldfarb-shanno

In Fig. 17, it can be observed that the meta-model LR achieved the best discriminative performance when the penalty coefficient (C_{LR}) was set to 1.0. In summary, the selected model hyperparameters are shown in Table 5.

3.4 Results and evaluation

In Section 3.3, we described how the accuracy evaluation metric was used for hyperparameter tuning, which focuses on the overall classification accuracy of the model without considering the differences between categories. To account for the performance of each category, we introduced the $F_{1,\mathrm{macro}}$ metric, which combines the precision and recall for each category.

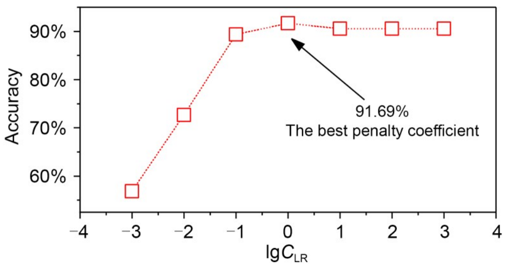

Fig. 17 Results for the LR model

Table 5 Values of model hyperparameters

Model	Hyperparameter	Description
KNN	$n_{\mathrm{neighbors}}$	7
RF	$n_{\mathrm{estimators}}$, $d_{\max}$	40, 4
SVC	C_{svc}, γ	1000, 0.001
ML	Solver, neuron_size	ADAM, (60)
LR	C_{LR}	1.0

The $F_{1,\mathrm{macro}}$ calculates the F_1 score for each category and then averages their performance to obtain a comprehensive performance measure. The calculation formulas are:

$$\begin{aligned} P_{\mathrm{macro}} &= \frac{1}{n}\sum_{i=1}^{n} P_i, \\ R_{\mathrm{macro}} &= \frac{1}{n}\sum_{i=1}^{n} R_i, \\ F_{1,\mathrm{macro}} &= \frac{2\times P_{\mathrm{macro}}\times R_{\mathrm{macro}}}{P_{\mathrm{macro}}+R_{\mathrm{macro}}}, \end{aligned} \tag{3}$$

where P_i denotes the precision rate for each category; R_i is the recall rate for each category; n is the number of categories; P_{macro} and R_{macro} represent the average precision and recall across all categories, respectively.

The results of the model comparison are presented in Fig. 18. It can be observed that PRDM achieved the highest values for both accuracy, which emphasizes classification accuracy, and $F_{1,\mathrm{macro}}$, which focuses on

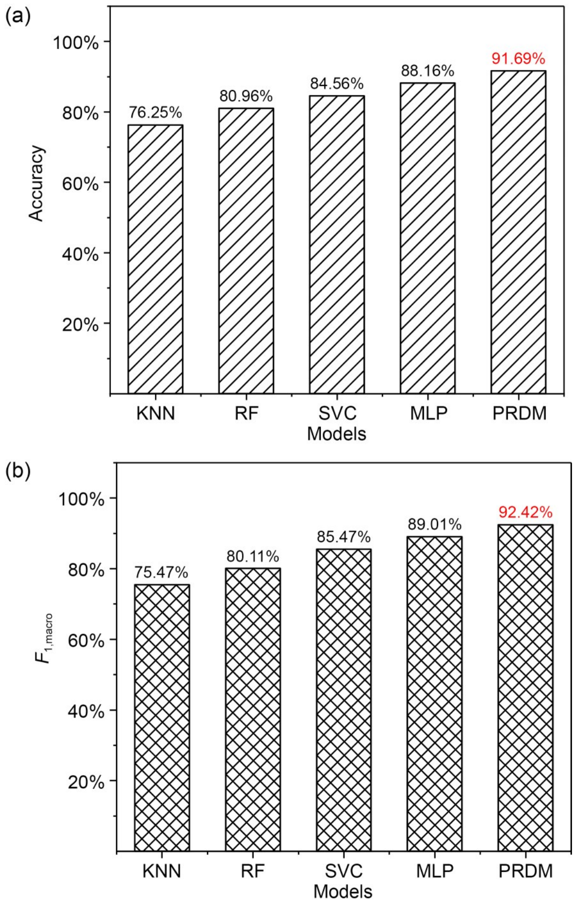

Fig. 18 Comparison results of the models: (a) accuracy; (b) $F_{1,\text{macro}}$

the overall performance and balance across multiple classes, with values of 91.69% and 92.42%, respectively. This indicates that the PRDM model can accurately discriminate partial-wear ratio. Additionally, to investigate the model's classification performance for each partial-wear ratio, we plotted the receiver operating characteristic (ROC) curves for each category and calculated the average area under the ROC curve (AUC) for each category, as shown in Fig. 19. As the partial-wear ratio increases, the model's discrimination performance improves, even reaching 100% accuracy at a partial-wear ratio of 75%. This further demonstrates that as the partial-wear ratio increases, the changes in torque and thrust become more pronounced, making their associated features more prominent. Furthermore, we calculated the macro-average ROC, which focuses on the model's ability to differentiate and accurately classify different classes, and it also achieved 95%.

In conclusion, evaluation and comparative analysis revealed the outstanding discriminatory performance of the PRDM model, which is built on the multi-domain features and stacking ensemble learning. This demonstrates its value as a tool for detection and early warning of disc-cutter failure in TBM operations.

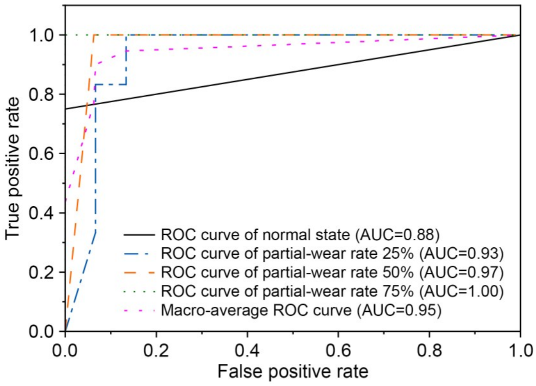

Fig. 19 ROC curves of PRDM

4 Conclusions

In this study, we conducted a series of shield-tunneling experiments on normal disc cutters and disc cutters with a certain proportion of partial wear and different partial-wear depth, aiming to investigate the variation in tunneling parameters and propose an accurate method for discriminating disc-cutter partial-wear ratio. Based on the experimental results, we can draw the following key conclusions:

(1) When abnormal damage occurs to normal disc cutters in the cutterhead, the torque and thrust in tunneling parameters increase. This is attributed to the change in the motion mode between the disc cutters and the rock (from rolling to sliding) and the alteration of the geometric profile of the disc-cutter rings.

(2) The increase in partial-wear ratio, i.e., the increase in the number of partially worn cutters, has a much greater impact on tunneling parameters compared to partial-wear depth. With a higher partial-wear ratio, the mean values of torque and thrust significantly increase. In contrast, at the same partial-wear ratio, the increase in partial-wear depth causes only a small change in the magnitude of the mean values of torque and thrust. This may be because the change in the motion mode has a higher impact than the alteration in the geometric profile.

(3) Partial-wear depth has a relatively small influence on the cyclic fluctuation of torque and thrust.

Standard deviations may even decrease with an increase in partial-wear depth, given the same partial-wear ratio. This is because the enlargement of the contact area between the partial-wear disc cutter and the rock does not affect the stability of the contact.

(4) There is a certain degree of correlation between time-domain, frequency-domain, and time-frequency domain features and the partial-wear ratio. The magnitude of Pearson correlation coefficients indicates the linear correlations between 28 features such as RMS, CF, and sub-band energy and the partial-wear ratio, while the magnitude of CE confirms the non-linear correlations between 12 features such as skewness and kurtosis and the partial-wear ratio.

(5) The proposed PRDM model can accurately discriminate the partial-wear ratio. Compared to models such as KNN, RF, SVC, and MLP, PRDM performs the best in terms of accuracy and $F_{1,\text{macro}}$ evaluation metrics. Analysis of ROC curves also demonstrates that the model exhibits good discrimination and judgment accuracy on different partial-wear ratios.

Future work will focus on investigating the impact of partial wear on tunneling parameters under different geological conditions. Additionally, we hope to explore the application of the proposed model in engineering projects in further studies.

Acknowledgments

This work is supported by the Natural Science Basic Research Program of Shaanxi Province (No. 2019JLZ-13), the National Key R&D Program of China (No. 2022YFC3802305), the National Natural Science Foundation of China (No. 52105074), and the Open Project of State Key Laboratory of Shield Machine and Boring Technology (No. SKLST-2021-K02), China.

Author contributions

Xinghai ZHOU designed the research and wrote the first draft of the manuscript. Yakun ZHANG designed the research and processed the corresponding data. Guofang GONG and Huayong YANG helped to organize the manuscript. Xinghai ZHOU revised and edited the final version.

Conflict of interest

Xinghai ZHOU, Yakun ZHANG, Guofang GONG, and Huayong YANG declare that they have no conflict of interest.

Reference

Acaroglu O, Ozdemir L, Asbury B, 2008. A fuzzy logic model to predict specific energy requirement for TBM performance prediction. *Tunnelling and Underground Space Technology*, 23(5):600-608.
https://doi.org/10.1016/j.tust.2007.11.003

Amoun S, Sharifzadeh M, Shahriar K, et al., 2017. Evaluation of tool wear in EPB tunneling of Tehran Metro, Line 7 Expansion. *Tunnelling and Underground Space Technology*, 61:233-246.
https://doi.org/10.1016/j.tust.2016.11.001

Bilgin N, Algan M, 2012. The performance of a TBM in a squeezing ground at Uluabat, Turkey. *Tunnelling and Underground Space Technology*, 32:58-65.
https://doi.org/10.1016/j.tust.2012.05.004

Cui S, Sun S, 2022. Study on the correlation of wind turbine variables under different conditions. *Integrated Intelligent Energy*, 44(12):49-55 (in Chinese).
https://doi.org/10.3969/j.issn.2097-0706.2022.12.007

Farrokh E, Rostami J, 2008. Correlation of tunnel convergence with TBM operational parameters and chip size in the Ghomroud tunnel, Iran. *Tunnelling and Underground Space Technology*, 23(6):700-710.
https://doi.org/10.1016/j.tust.2008.01.005

Hassanpour J, 2018. Development of an empirical model to estimate disc cutter wear for sedimentary and low to medium grade metamorphic rocks. *Tunnelling and Underground Space Technology*, 75:90-99.
https://doi.org/10.1016/j.tust.2018.02.009

Hassanpour J, Rostami J, Tarigh Azali S, et al., 2014. Introduction of an empirical TBM cutter wear prediction model for pyroclastic and mafic igneous rocks; a case history of Karaj water conveyance tunnel, Iran. *Tunnelling and Underground Space Technology*, 43:222-231.
https://doi.org/10.1016/j.tust.2014.05.007

Hou SK, Liu YR, Yang Q, 2022. Real-time prediction of rock mass classification based on TBM operation big data and stacking technique of ensemble learning. *Journal of Rock Mechanics and Geotechnical Engineering*, 14(1):123-143.
https://doi.org/10.1016/j.jrmge.2021.05.004

Huang H, Yao JJ, Xue WH, et al., 2022. Tool wear state recognition based on joint distribution adaptation of multi-domain feature. *Computer Integrated Manufacturing Systems*, 28(8):2419-2429 (in Chinese).
https://doi.org/10.13196/j.cims.2022.08.013

Huang J, 2021. Application and research of composite shield disc cutter in quartzite stratum excavation. *Construction Technology*, 50(11):124-128 (in Chinese).
https://doi.org/10.7672/sgjs2021110124

Jiang YL, Liu QS, Zhu BT, et al., 2022. Correlation analysis of machine performance parameters and rock mass properties during tunnel boring machine excavation process: a case study in Yin-song headrace tunnel, China. *Journal of Testing and Evaluation*, 50(6):2883-2900.
https://doi.org/10.1520/JTE20200639

Karami M, Zare S, Rostami J, 2021. Tracking of disc cutter wear in TBM tunneling: a case study of Kerman water conveyance tunnel. *Bulletin of Engineering Geology and the Environment*, 80(1):201-219.
https://doi.org/10.1007/s10064-020-01931-7

Ko TY, Lee SS, 2020. Effect of rock abrasiveness on wear of shield tunnelling in Bukit Timah granite. *Applied Sciences*, 10(9):3231.
https://doi.org/10.3390/app10093231

Labra C, Rojek J, Oñate E, 2017. Discrete/finite element modelling of rock cutting with a TBM disc cutter. *Rock Mechanics and Rock Engineering*, 50(3):621-638.
https://doi.org/10.1007/s00603-016-1133-7

Lan H, Xia YM, Ji ZY, et al., 2019. Online monitoring device of disc cutter wear–design and field test. *Tunnelling and Underground Space Technology*, 89:284-294.
https://doi.org/10.1016/j.tust.2019.04.010

Li J, Nie YF, Fu K, et al., 2018. Experiment and analysis of the rock breaking characteristics of disc cutter ring with small edge angle in high abrasive grounds. *Journal of the Brazilian Society of Mechanical Sciences and Engineering*, 40(10):505.
https://doi.org/10.1007/s40430-018-1422-z

Li X, Su XJ, 2010. A new method for forecasting shield's disc-cutters wearing based on Elman neural network. *Journal of Liaoning Technical University (Natural Science Edition)*, 29(6):1121-1124 (in Chinese).
https://doi.org/10.3969/j.issn.1008-0562.2010.06.030

Li YZ, 2021. Failure form and cause analysis of EPB shield cutter in a water diversion project in Xinjiang. *Modern Manufacturing Technology and Equipment*, 57(9):51-54 (in Chinese).
https://doi.org/10.16107/j.cnki.mmte.2021.0712

Lin LK, Xia YM, Zhang XH, 2020. Wear characteristics of TBM disc cutter ring sliding against different types of rock. *KSCE Journal of Civil Engineering*, 24(10):3145-3155.
https://doi.org/10.1007/s12205-020-2208-2

Liu BL, Yang HQ, Karekal S, 2021. Reliability analysis of TBM disc cutters under different conditions. *Underground Space*, 6(2):142-152.
https://doi.org/10.1016/j.undsp.2020.01.001

Liu Z, Wang B, Shang W, 2017. Study of wireless detection system of shield cutter wear based on ultrasonic. *Tunnel Construction*, 37(11):1469-1474.
https://doi.org/10.3973/j.issn.2096-4498.2017.11.017

Pan YC, Liu QS, Liu Q, et al., 2020. Full-scale linear cutting tests to check and modify a widely used semi-theoretical model for disc cutter cutting force prediction. *Acta Geotechnica*, 15(6):1481-1500.
https://doi.org/10.1007/s11440-019-00852-4

Qin CJ, Wu RH, Huang GQ, et al., 2023. A novel LSTM-autoencoder and enhanced transformer-based detection method for shield machine cutterhead clogging. *Science China Technological Sciences*, 66(2):512-527.
https://doi.org/10.1007/s11431-022-2218-9

Ren DJ, Shen SL, Arulrajah A, et al., 2018. Prediction model of TBM disc cutter wear during tunnelling in heterogeneous ground. *Rock Mechanics and Rock Engineering*, 51(11):3599-3611.
https://doi.org/10.1007/s00603-018-1549-3

Rostami J, 2013. Study of pressure distribution within the crushed zone in the contact area between rock and disc cutters. *International Journal of Rock Mechanics and Mining Sciences*, 57:172-186.
https://doi.org/10.1016/j.ijrmms.2012.07.031

She L, Zhang SR, Wang C, et al., 2022. A cutting mechanics model of constant cross-section type disc cutter and its application based on dense core theory. *International Journal of Rock Mechanics and Mining Sciences*, 150: 105025.
https://doi.org/10.1016/j.ijrmms.2021.105025

Shi ML, Hu WF, Li MX, et al., 2023. Ensemble regression based on polynomial regression-based decision tree and its application in the in-situ data of tunnel boring machine. *Mechanical Systems and Signal Processing*, 188:110022.
https://doi.org/10.1016/j.ymssp.2022.110022

Su WL, Li XG, Jin DL, et al., 2020. Analysis and prediction of TBM disc cutter wear when tunneling in hard rock strata: a case study of a metro tunnel excavation in Shenzhen, China. *Wear*, 446-447:203190.
https://doi.org/10.1016/j.wear.2020.203190

Sun RX, Mo JL, Zhang MQ, et al., 2022. Cutting performance and contact behavior of partial-wear TBM disc cutters: a laboratory scale investigation. *Engineering Failure Analysis*, 137:106253.
https://doi.org/10.1016/j.engfailanal.2022.106253

Sun RX, Mo JL, Zhang MQ, et al., 2023. Interaction between partial-worn TBM cutters and rocks: experimental and numerical investigation. *Bulletin of Engineering Geology and the Environment*, 82(4):111.
https://doi.org/10.1007/s10064-023-03127-1

Wang F, Men C, Kong XW, et al., 2019. Optimum design and application research of eddy current sensor for measurement of TBM disc cutter wear. *Sensors*, 19(19):4230.
https://doi.org/10.3390/s19194230

Wang YX, Gao XC, Jiang P, et al., 2022. An extreme gradient boosting technique to estimate TBM penetration rate and prediction platform. *Bulletin of Engineering Geology and the Environment*, 81(1):58.
https://doi.org/10.1007/s10064-021-02527-5

Yang HQ, Liu BL, Wang YQ, et al., 2021. Prediction model for normal and flat wear of disc cutters during TBM tunneling process. *International Journal of Geomechanics*, 21(3):10.
https://doi.org/10.1061/(ASCE)GM.1943-5622.0001950

Yang JZ, Qiu CY, 2016. Prediction of cutting tool wear rate. *Construction Technology*, 45(22):25-30 (in Chinese).
https://doi.org/10.7672/sgjs2016220025

Yang ZX, Wang LQ, Zhou JJ, et al., 2023. Mechanical characteristics of a tunnel boring machine cutterhead during rock breaking: physical model tests and transient dynamic analysis. *Advances in Mechanical Engineering*, 15(3): 1-11.
https://doi.org/10.1177/16878132231159971

Yu HG, Tao JF, Huang S, et al., 2021. A field parameters-based method for real-time wear estimation of disc cutter on TBM cutterhead. *Automation in Construction*, 124: 103603.
https://doi.org/10.1016/j.autcon.2021.103603

Yu HG, Qin CJ, Tao JF, et al., 2023. A multi-channel decoupled deep neural network for tunnel boring machine

torque and thrust prediction. *Tunnelling and Underground Space Technology*, 133:104949.
https://doi.org/10.1016/j.tust.2022.104949

Yu QZ, Long WY, Yang XY, et al., 2020. Effects of heat treatment process with different hardness gradients on microstructure and mechanical properties of shield cutter ring. *Hot Working Technology*, 12(49):150-152 (in Chinese).
https://doi.org/10.14158/j.cnki.1001-3814.20193719

Zhang GJ, Xiao CY, 2018a. Analysis of thermal stress distribution of TBM disc cutter. *Australian Journal of Mechanical Engineering*, 16:43-48.
https://doi.org/10.1080/1448837X.2018.1545471

Zhang GJ, Xiao CY, 2018b. Analysis of stress distribution of disc cutter under different tunnelling parameters. *Australian Journal of Mechanical Engineering*, 16:49-53.
https://doi.org/10.1080/1448837X.2018.1545472

Zhang HM, 2011. Mechanical analysis of TBM disc cutter damage mechanism and its application. *Modern Tunnelling Technology*, 48(1):61-65 (in Chinese).
https://doi.org/10.13807/j.cnki.mtt.2011.01.018

Zhang N, Shen SL, Zhou AN, 2023. A new index for cutter life evaluation and ensemble model for prediction of cutter wear. *Tunnelling and Underground Space Technology*, 131:104830.
https://doi.org/10.1016/j.tust.2022.104830

Zhang XH, Xia YM, Zhang YC, et al., 2017. Experimental study on wear behaviors of TBM disc cutter ring under drying, water and seawater conditions. *Wear*, 392-393:109-117.
https://doi.org/10.1016/j.wear.2017.09.020

Zhang YC, 2021. Design and Research of Test Platform for Thrust Hydraulic Cylinder in Shield Machine. MS Thesis, China University of Mining and Technology, Xuzhou, China (in Chinese).

Electronic supplementary materials

Sections S1–S4